

# Spacecraft and interplanetary contributions to the magnetic environment on-board LISA Pathfinder

M. Armano,<sup>1</sup> H. Audley,<sup>2</sup> J. Baird,<sup>3</sup> P. Binetruy,<sup>3†</sup> M. Born,<sup>2</sup> D. Bortoluzzi,<sup>4</sup> E. Castelli,<sup>5</sup> A. Cavalleri,<sup>6</sup> A. Cesarini,<sup>7</sup> A. M. Cruise,<sup>8</sup> K. Danzmann,<sup>2</sup> M. de Deus Silva,<sup>9</sup> I. Diepholz,<sup>2</sup> G. Dixon,<sup>8</sup> R. Dolesi,<sup>5</sup> L. Ferraioli,<sup>9</sup> V. Ferroni,<sup>5</sup> E. D. Fitzsimons,<sup>10</sup> M. Freschi,<sup>11</sup> L. Gesa,<sup>12</sup> F. Gibert,<sup>5</sup> D. Giardini,<sup>9</sup> R. Giusteri,<sup>5</sup> C. Grimani,<sup>7</sup> J. Grzysch,<sup>1</sup> I. Harrison,<sup>13</sup> M.-S. Hartig,<sup>2</sup> G. Heinzel,<sup>2</sup> M. Hewitson,<sup>2</sup> D. Hollington,<sup>14</sup> D. Hoyland,<sup>8</sup> M. Hueller,<sup>5</sup> H. Inchauspé,<sup>3,15</sup> O. Jennrich,<sup>1</sup> P. Jetzer,<sup>16</sup> N. Karnesis,<sup>3</sup> B. Kaune,<sup>2</sup> N. Korsakova,<sup>17</sup> C. J. Killow,<sup>17</sup> J. A. Lobo,<sup>12‡</sup> L. Liu,<sup>5</sup> J. P. López-Zaragoza,<sup>12★</sup> R. Maarschalkerweerd,<sup>13</sup> D. Mance,<sup>9</sup> V. Martín,<sup>12</sup> L. Martín-Polo,<sup>11</sup> J. Martino,<sup>3</sup> F. Martin-Porqueras,<sup>11</sup> I. Mateos,<sup>12</sup> P. W. McNamara,<sup>1</sup> J. Mendes,<sup>13</sup> L. Mendes,<sup>11</sup> N. Meshksar,<sup>9</sup> M. Nofrarias,<sup>12★</sup> S. Paczkowski,<sup>2</sup> M. Perreux-Lloyd,<sup>17</sup> A. Petiteau,<sup>3</sup> P. Pivato,<sup>5</sup> E. Plagnol,<sup>3</sup> J. Ramos-Castro,<sup>18</sup> J. Reiche,<sup>2</sup> F. Rivas,<sup>12</sup> D. I. Robertson,<sup>17</sup> D. Roma-Dollase,<sup>12</sup> G. Russano,<sup>5</sup> J. Slutsky,<sup>2</sup> C. F. Sopena,<sup>12</sup> T. Sumner,<sup>14</sup> D. Telloni,<sup>19</sup> D. Texier,<sup>11</sup> J. I. Thorpe, C. Trenkel,<sup>20</sup> D. Vetrugno,<sup>5</sup> S. Vitale,<sup>5</sup> G. Wanner,<sup>2</sup> H. Ward,<sup>17</sup> P. J. Wass,<sup>14</sup> D. Wealthy,<sup>20</sup> W. J. Weber,<sup>5</sup> L. Wissel,<sup>2</sup> A. Wittchen<sup>2</sup> and P. Zweifel<sup>9</sup>

*Affiliations are listed at the end of the paper*

Accepted 2020 March 18. Received 2020 March 15; in original form 2020 January 28

## ABSTRACT

LISA Pathfinder (LPF) has been a space-based mission designed to test new technologies that will be required for a gravitational wave observatory in space. Magnetically driven forces play a key role in the instrument sensitivity in the low-frequency regime (mHz and below), the measurement band of interest for a space-based observatory. The magnetic field can couple to the magnetic susceptibility and remanent magnetic moment from the test masses and disturb them from their geodesic movement. LPF carried on-board a dedicated magnetic measurement subsystem with noise levels of  $10 \text{ nT Hz}^{-1/2}$  from 1 Hz down to 1 mHz. In this paper we report on the magnetic measurements throughout LPF operations. We characterize the magnetic environment within the spacecraft, study the time evolution of the magnetic field and its stability down to  $20 \mu\text{Hz}$ , where we measure values around  $200 \text{ nT Hz}^{-1/2}$ , and identify two different frequency regimes, one related to the interplanetary magnetic field and the other to the magnetic field originating inside the spacecraft. Finally, we characterize the non-stationary component of the fluctuations of the magnetic field below the mHz and relate them to the dynamics of the solar wind.

**Key words:** gravitational waves – magnetic fields – space vehicles: instruments.

## 1 INTRODUCTION

LISA Pathfinder (LPF; Anza et al. 2005; Antonucci et al. 2012) was an ESA mission with NASA contributions designed to test key technologies for the future gravitational wave observatory in

\* E-mail: [jplovez@ice.cat](mailto:jplovez@ice.cat) (JPLZ); [nofrarias@ice.cat](mailto:nofrarias@ice.cat) (MN)

† Deceased 30 March 2017

‡ Deceased 30 September 2012

space, the Laser Interferometry Space Antenna (LISA) (Amaro-Seoane et al. 2017). The main scientific goal for the mission was to reach a relative acceleration noise between two test masses in nominal geodesic motion of  $3 \times 10^{-14} \text{ m s}^{-2} \text{ Hz}^{-1/2}$  at 1 mHz. The relevance of this measurement was not only its demand in terms of noise reduction but also the very low-frequency measuring band, which introduces technological difficulties that cannot be addressed by ground-based gravitational wave detectors.

LPF was successfully launched on 2015 December 3, and started scientific operations after arriving at the Lagrange point L1 on 2016 March 1. The mission plan included a six-month operation split between the two experiments on-board: the European LISA Technology Package (LTP) and the American Disturbance Reduction System (DRS). LPF achieved residual acceleration noise levels of  $1.74 \pm 0.01 \text{ fm s}^{-2} \text{ Hz}^{-1/2}$  between 2 and 20 mHz, and  $60 \pm 10 \text{ fm s}^{-2} \text{ Hz}^{-1/2}$  at  $20 \mu\text{Hz}$  (Armano et al. 2016, 2018b), which went beyond the required performance and, hence, successfully demonstrated the technology to detect gravitational waves in space.

Apart from achieving a high level of free fall, it is also important to understand the different contributions that will build up the instrument noise model. Therefore, one of the main objectives of LPF is to split up the noise into different contributions and help on the design of a suitable environment for future gravitational wave detectors. With that aim, LPF carried the so-called Data and Diagnostics Subsystem (DDS), which includes a temperature measurement subsystem (Sanjuán et al. 2007; Armano et al. 2019b), a magnetic diagnostic subsystem (Diaz-Aguiló et al. 2013), and a radiation monitor (Canizares et al. 2009, 2011; Armano et al. 2018a).

In this work we focus on the results of the magnetic diagnostics and more specifically on the characterization of the environment on-board the spacecraft during mission operations. Understanding the variability of the magnetic environment is crucial for future spaceborne gravitational wave detectors since any magnetic perturbation has a potential impact on the instrument performance through magnetic induced forces exerted on the test masses. With that aim, both interplanetary and platform originated magnetic fluctuations must be considered and characterized.

This work is organized as follows. In Section 2 we introduce the nature of the magnetic forces that can perturb the test mass motion and describe the magnetic diagnostic system on-board, designed to study and disentangle this contribution. In Section 3 we describe the in-flight measurements and characterize the magnetic environment on-board as measured by the LPF magnetometers. Finally, we present our conclusions in Section 4.

## 2 THE ROLE OF THE MAGNETIC ENVIRONMENT IN LISA PATHFINDER

The geodesic motion of the test masses on-board LPF is subjected to several sources of disturbance. Some of them can be corrected through the control loops that prevent, for instance, the push from solar radiation pressure to depart the mass from its free-fall orbit. Other sources of disturbance, however, cannot be prevented and need to be studied and characterized carefully since they will become an inherent part of the instrument noise budget. This is the case of the forces of magnetic origin applied on the test mass.

Indeed, an important contribution in the instrument budget is a force on the test mass that can arise due to variations in the magnetic field on the test masses location, originating a magnetic force on the test mass that could not be discriminated from a force of gravitational origin.

### 2.1 Magnetic forces on the test mass

To understand the coupling of the test mass to magnetic induced forces one can consider the test mass inside the spacecraft as a magnetic dipole in a magnetic field. In such approximation, the test mass will sense a force given by

$$\mathbf{F} = \langle \mathbf{M} \cdot \nabla \mathbf{B} \rangle V, \quad (1)$$

where  $\mathbf{M}$  is the intrinsic moment of the magnetic dipole,  $\mathbf{B}$  the surrounding magnetic field and  $V$  the test mass volume. Here we use the brackets as an average over the test mass volume. For the sake of simplicity we do not take into account inhomogeneities or anisotropies in the composition of the test mass. A more detailed model of the effect of magnetic field on the test mass would consider also torques applied to the test mass (Diaz-Aguiló, García-Berro & Lobo 2012). Several considerations need to be taken into account for the free-falling test masses inside the satellite. First, two contributions to the magnetic moment need to be distinguished: a first one from the intrinsic remanent magnetic moment ( $\mathbf{M}_r$ ) and a second one coming from induced magnetic moment, which is proportional (through the magnetic susceptibility,  $\chi$ ) to the applied magnetic field ( $\mathbf{M}_i = \chi \mu_0^{-1} \mathbf{B}$ ). Both contributions are determined by the composition of the test mass, which in the LPF case was a Pt (27 per cent) and Au (73 per cent) alloy. Equation (1) therefore expands to

$$\mathbf{F} = \left\langle \left[ \mathbf{M}_r + \frac{\chi}{\mu_0} \mathbf{B} \right] \cdot \nabla \mathbf{B} \right\rangle V. \quad (2)$$

Since the main objective of the mission is to understand differential acceleration fluctuations down to the mHz, we further need to consider how fluctuations of the magnetic field will impact on the force. The different components to this contribution can be easily visualized if one splits both the magnetic field and the magnetic field gradient into a constant contribution and a term that varies with time

$$\mathbf{B} = \mathbf{B}_0 + \delta \mathbf{B}$$

$$\nabla \mathbf{B} = \nabla \mathbf{B}_0 + \delta \nabla \mathbf{B},$$

which leads to several magnetically-induced force contributions

$$\begin{aligned} \mathbf{F} = & \left[ \langle \mathbf{M}_r \cdot \nabla \mathbf{B}_0 \rangle + \langle \mathbf{M}_r \cdot \delta \nabla \mathbf{B}_0 \rangle \right] V \\ & + \left\langle \frac{\chi}{\mu_0} [\mathbf{B}_0 \cdot \nabla \mathbf{B}_0 + \mathbf{B}_0 \cdot \delta \nabla \mathbf{B}] \right\rangle V \\ & + \left\langle \frac{\chi}{\mu_0} [\delta \mathbf{B} \cdot \nabla \mathbf{B}_0 + \delta \mathbf{B} \cdot \delta \nabla \mathbf{B}] \right\rangle V. \end{aligned} \quad (3)$$

From equation (3) we clearly observe how the magnetic environment will induce a variety of effects on the test mass that include: constant force contributions ( $\mathbf{B}_0 \cdot \nabla \mathbf{B}_0$ ); terms that will couple the local field at the test mass position to the fluctuations of the gradient of the magnetic field ( $\mathbf{B}_0 \cdot \delta \nabla \mathbf{B}$ ); couplings of the local magnetic field gradient to fluctuations in the magnetic field ( $\delta \mathbf{B} \cdot \nabla \mathbf{B}_0$ ) and coupling of fluctuations in the field and its gradient ( $\delta \mathbf{B} \cdot \delta \nabla \mathbf{B}$ ). Hence, equally important for the experiment are both the monitoring of magnetic field and magnetic field fluctuations since both can couple, through the test mass remanent magnetic moment and susceptibility, into spurious accelerations of the free-falling test masses. We will describe in the following the diagnostics subsystem used on-board to characterize these figures to later describe the results obtained with these sensors.

## 2.2 The magnetic diagnostics subsystem

The LPF magnetic diagnostics subsystem fulfils two related purposes. First, to measure the magnetic field and magnetic field gradient on-board and second, to create magnetic fields and gradients at the position of the test masses to study the contribution of the magnetic forces to the instrument noise budget. The subsystem is therefore composed by four tri-axial magnetometers and two induction coils to fulfil these two purposes, respectively.

The coils are capable of generating a controlled magnetic field at the location of the test masses. The two circular induction coils are located 85.5 mm away from the test mass, each one attached to the external wall of each vacuum enclosure. The coils have a radius of 56.5 mm and are built with 2400 windings of a copper alloy mounted on a titanium support with a dedicated high stability current driver to ensure that high-precision magnetic forces are produced (Diaz-Aguiló et al. 2013). The coils are aligned with the axis joining both test masses so that the generated magnetic field has axial symmetry. Experiments conducted to study magnetically-induced forces on the test masses during flight operations will be reported in a separate publication.

The magnetometers are intended to sense with high precision the evolution of the magnetic field. The magnetometers on-board LPF are fluxgate tri-axial magnetometers, namely TFM100G4-VQS from Billingsley with a sensitivity of  $166.7 \mu\text{V/nT}$  and a typical root-mean-square noise figure of  $20 \text{ pT/Hz}$  at 1 Hz. In fluxgate magnetometers, each axis consists of a first sensing coil surrounding a second inner drive coil wound around a high permeability magnetic core material. Although providing low-noise measurements, because of the active magnetic core inside the sensor, these magnetometers have to be located far enough from the test mass position so they do not contribute as a source of magnetically-induced force on the test mass. All magnetometers channels are connected to a multiplexer after passing through an analogue low-pass filter. The signal is then amplified by means of discrete operational amplifiers (OP471AY/QMLR) in an instrumentation amplifier configuration. Finally, it is digitally converted by a 16-bit analogue-to-digital converter (7809LPRPFH). The sampling frequency is 50 Hz. Hence, since the input is multiplexed by 16 channels, the individual channel sampling frequency is 3.125 Hz. In Section 3.2.3 we will come back to the two last components of the read-out chain, instrumentation amplifier and analogue-to-digital converter, which determine the noise performance of the magnetometer read-out.

In terms of data handling, the magnetometers data were downloaded with a dedicated telemetry package, which also included all the diagnostics on-board the satellite. This approach is a characteristic of LPF and differs from most of the scientific space missions where the diagnostics subsystem is considered only for house-keeping purposes. The rationale behind this is that, in gravitational wave detectors, noise characterization and noise hunting is crucial for the operation of the instrument. Hence, in our current case, environment sensors entail key information for the achievement of the scientific goal.

## 3 IN-FLIGHT MEASUREMENTS

After a one-month cruise phase, LPF reached the L1 Lissajous orbit in 2016 January. The magnetometers on-board started collecting data on January 11th, at the start of the LTP commissioning phase and, apart from some short outages events, they acquired data uninterruptedly until the end of the scientific operations in 2017 July.

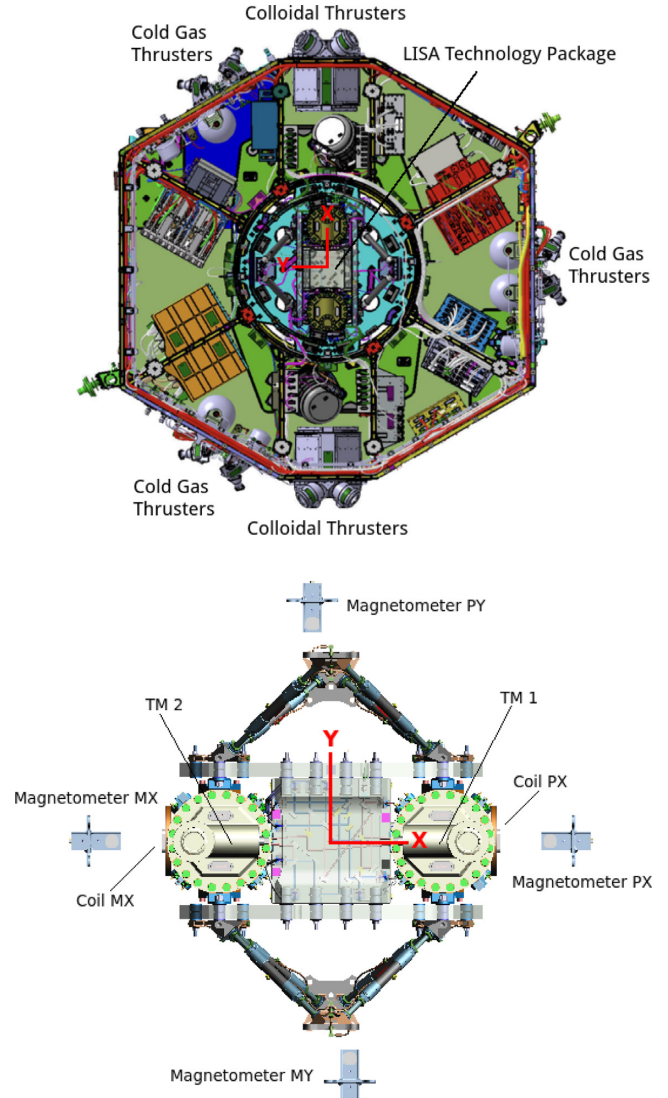


**Figure 1.** *Top:* X–Y plane view of the LPF spacecraft with the solar panel removed. The positions of the three sets of Cold Gas thrusters and the two sets of Colloidal Thrusters are indicated, as well as the LISA Technology Package in the centre of the spacecraft. The LPF reference frame is shown in red, with its origin in the middle of the LISA Technology Package. *Bottom:* Zoom of the LISA Technology Package from the upper figure. Here we show the position of several items from the Data Diagnostics Subsystem, consisting of two coils and four tri-axial fluxgate magnetometers. In this notation ‘P’ stands for ‘plus’ and ‘M’ for ‘minus’, being each element named according to their position within the satellite reference frame. The position of both test masses is also indicated, as well as the LPF reference frame, like in the upper figure.

Contrary to many other missions that carry their magnetometers at the end of a long boom to isolate the measurement from spacecraft interferences, magnetometers on-board LPF are located inside the spacecraft with the main objective of monitoring the magnetic field as close as possible to the test mass position. At the same time, the magnetometers have to be sufficiently far away from the test masses since, as explained before, the fluxgate head contains a magnetically active component that could induce spurious forces on the test mass, therefore disturbing the main scientific measurement of the mission. The trade-off between these two conditions results in the locations shown in Fig. 1.

All magnetometers are located in the plane defined by the test masses and the optical bench. This configuration allows for an approximate estimate of the magnetic field gradient, a key factor in the magnetic noise contribution to the test masses free fall, across two axes but it leaves the third one, Z in the spacecraft frame, unmeasured. It is worth stressing that the gradients estimated that way are unlikely to be representative of the magnetic field gradient at the test mass position, the reason being that local sources, as for instance the temperature sensors surrounding the test masses in the electrode housing, could be a potential source of local magnetic gradient (Sanjuan et al. 2009). For instance, for the worst-case layout of these sensors, the magnetic field gradient across X between the two faces of the test masses could reach values around  $10 \mu\text{T m}^{-1}$ , which would be orders of magnitude above the values we report in Appendix A for the gradients computed across magnetometers. As we will show in the following, the DC value measured by each magnetometer is completely dominated by the spacecraft units while the fluctuations have both a spacecraft and an interplanetary contribution.

### 3.1 Evolution of the measured on-board magnetic field

In the top panel of Fig. 2 we show the time series for the read-out of the four magnetometers on-board LPF since the magnetometers switch-on and until the end of the mission, in 2017 July. We provide the magnetic field measurements in the X, Y, and Z axes in the LTP reference frame, although the X-component contains most of the interesting features that we will discuss in the following.

The absolute value of the magnetic field at each magnetometer location is dominated by the spacecraft contribution reaching values up to  $1 \mu\text{T}$ , far from typical interplanetary magnetic field values which would be of the order of 5–10 nT. Most of the magnetic field measured by the magnetometers corresponds to the contribution of the cold gas micropropulsion system, in particular to the magnets on the high-pressure latch valves. With an on-ground measured moment of  $950 \text{ mA m}^2$ , they account for most of the magnetic field measured by the magnetometers (Armano et al. 2015). It is important to mention that since the cold gas thrusters are placed in different locations of the spacecraft the magnetic field they create do not necessarily add in the same direction.

The time series can be divided in six different segments which correspond to the different phases of the mission, namely commissioning, LTP operations, DRS operations, the associated mission extension for both experiments, and decommissioning. The most prominent features in the magnetic field timeline are experiments with the coils to characterize the magnetic contribution to the test mass free fall. These experiments are listed in Table 1. Other features that affected the magnetic environment and can be identified in Fig. 2 are listed in Table 2. In the latter case, these are not associated to the activation of the coils on-board (except for event ‘a’, which was a check of the correct functioning of coil 2) but to the operation of the spacecraft itself, i.e. from changes in configuration to identified anomalies during operations. For the sake of completeness, the mean values of the magnetic field DC for different configurations of the spacecraft can be found in Appendix A.

In terms of the magnetic environment, we notice that DRS operations had an impact in the spacecraft magnetic environment. As seen in the bottom panel of Fig. 2, the mean value of the X component shows a steady decrease of  $150 \text{ nT}$  starting around August 8th and ending around November 13th. for the two magnetometers located near the test masses, i.e. magnetometers PX and MX in

the bottom panel of Fig. 1. This period is coincident with the start of operations of the DRS instrument. Apart from this long drift, in magnetometers PX and MX we also observe a DC increase of about  $40 \text{ nT}$  when we turn on the DRS system and the same decrease when we turn it off. This DC change should be related to some units being switched on and off when we change the control system of the satellite.

The reason of this long term trend observed in the magnetic field on-board can be explained by the differences between LTP and DRS micropropulsion systems. The LTP micropropulsion system consists of three clusters each featuring four cold gas thrusters (Armano et al. 2019a). The thruster system uses high-pressure Nitrogen propellant to provide very small impulses with a thrust range of 1–500  $\mu\text{N}$ . Four nitrogen tanks store the gas at 310 bar with a maximum capacity of 9.6 kg of nitrogen. The DRS micropropulsion system is composed by two Colloid Micro-Newton Thruster (CMNT) clusters (Ziemer et al. 2006). Each cluster includes four complete and independent thruster units. For the CMNT subsystem, thrust is adjustable from 5–30  $\mu\text{N}$  by changing the beam voltage and/or propellant flow rate that determines the beam current. In this case, the propellant is stored in four electrically isolated stainless steel bellows compressed by four constant force springs set to supply four microvalves with propellant at approximately 1 atm of pressure. In terms of the spacecraft magnetic field, this sets a relevant difference between both thrust subsystems since the continuous operation of the CMNT subsystem leads to a steady displacement of the bellows inside the storage tank. Although not having a direct impact on the mission operations in terms of gravitational pull, it is precisely this displacement of the stainless steel bellows occurring during the depletion of the fuel tanks the one that originates the observed magnetic field change. Indeed, given the known geometry and measured magnetic properties of the CMNT we can estimate the impact of the operation of these thrusters on the magnetic environment. The CMNT are aligned in the direction joining both test masses (X direction) as can be seen in the top panel of Fig. 1. They are located at a distance of 28 cm with respect to the two magnetometers that are located along this same axis, the PX and MX magnetometers in the notation of the bottom panel of Fig. 1. The measurement on-ground reported a magnetic moment for these units of  $209 \text{ mA m}^2$  (in modulus), which would produce a magnetic field of  $1.1 \mu\text{T}$  on the position of the closest magnetometer to each CMNT according to the equation of the magnetic field produced by a magnetic dipole

$$\mathbf{B}(\mathbf{r}) = \frac{\mu_0}{4\pi} \left( \frac{3\mathbf{r}(\mathbf{m} \cdot \mathbf{r})}{r^5} - \frac{\mathbf{m}}{r^3} \right) \quad (4)$$

with  $\mathbf{m}$  being the magnetic moment of the source and  $\mathbf{r}$  a vector going from the centre of the magnetic dipole to the position where the magnetic field is being measured. If we now assume that the overall variation in the magnetic field measured in the X direction during DRS operations is due to the displacement of the bellow inside the CMNT valves, this would imply a 1 cm displacement which is compatible with the geometry of the valve and the amount of propellant being expelled during this period.

### 3.2 Fluctuations of the on-board magnetic field

Given that any varying magnetic field or magnetic field gradient will couple into the motion of the test masses, understanding the origin of the fluctuations of the magnetic field measured on-board is an important output of LPF for future gravitational wave detectors in space. In the previous section we have seen how the

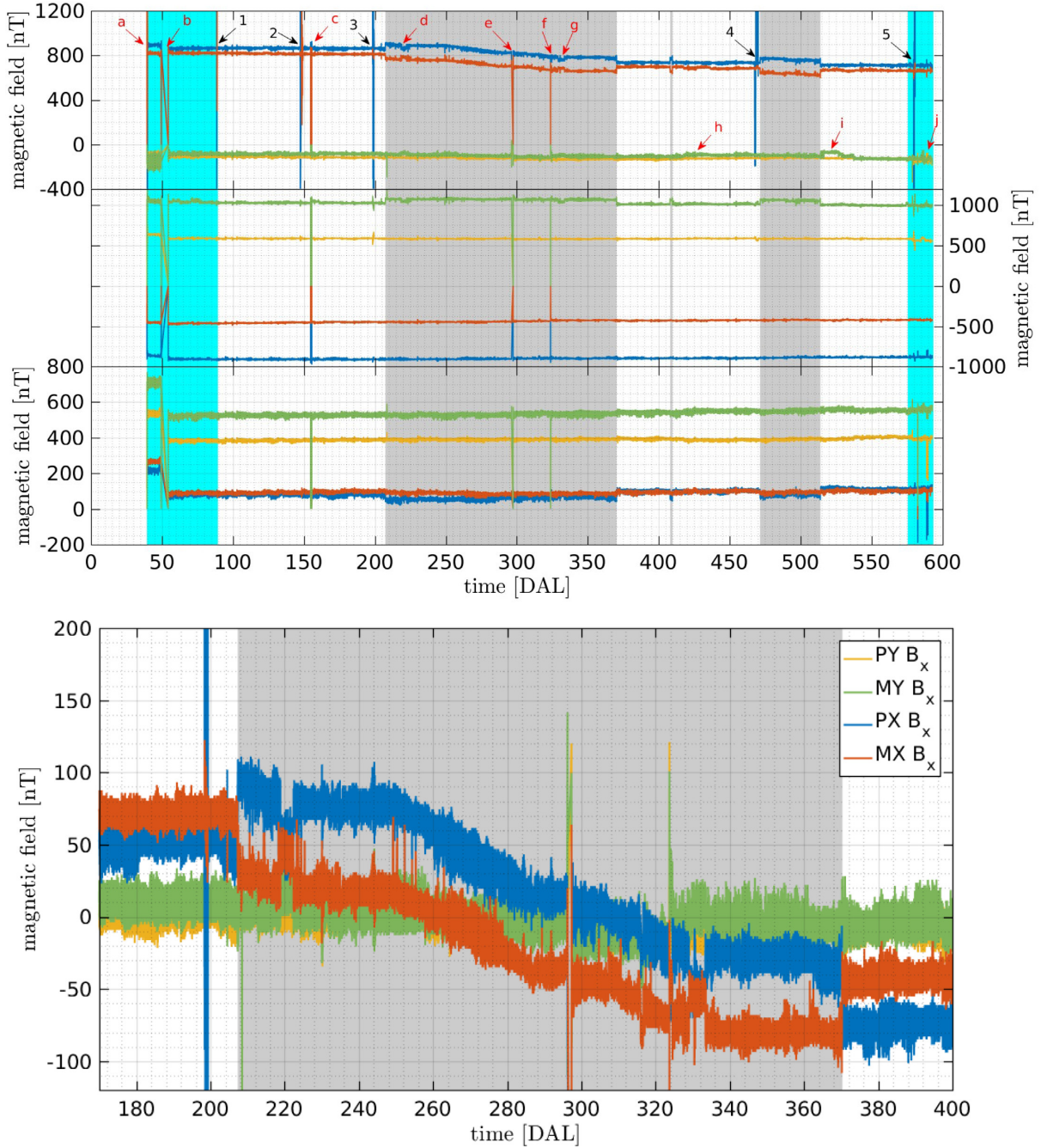


**Figure 2.** *Top:* Magnetic field measurements on-board LPF from launch date until the satellite passivation. The time axis is Days After Launch (DAL). The two cyan areas (DAL 40-90 and DAL 575-593) correspond to the commissioning and decommissioning periods, respectively. The three grey shadowed areas (DAL 210-370, DAL 414-415, and DAL 470-510) correspond to the DRS operations, and the rest correspond to LTP operations. From top to bottom panel: the X, Y, and Z components of the magnetic field, for magnetometers PX (blue), MX (red), PY (yellow), and MY (green). In this notation, ‘M’ stands for minus and ‘P’ for plus. ‘X’ and ‘Y’ refer to axes on-board in which the magnetometers are aligned, so PX and MX are the two closest magnetometers to the TMs. The arrows correspond to events related to important changes in magnetic field. These events are reported in Tables 1 and 2. *Bottom:* Zoom of X-component measurements for the four magnetometers during the first DRS operations period (2016 August–November). In this case, we removed the DC level from each channel to show all measurements in the same scale. See text for more detail.

electronic units on-board the satellite are the dominant contribution to the magnetometers DC measurement since the interplanetary contribution (typically of the order of 5–10 nT) is at least one order of magnitude below the values reported, for instance, in Table A1. The situation is different when we study the variations of the magnetic field. A wide variety of phenomena can produce a varying

magnetic field and, as we show in the following, both fluctuations originated by the spacecraft and by the interplanetary magnetic field are relevant to understand the magnetic field spectra measured by LPF.

We divide the three sections below as follows. First, we provide a characterization of the different magnitudes describing the

**Table 1.** Dates associated with magnetic experiments on-board LPF. In parenthesis we include the DAL.

Event	Date (DAL)
(1) Commissioning injections in TMs 1 & 2	28 Feb '16 (87)
(2) Mag. exps. in TMs 1 & 2	27 April '16 (146)
(3) Mag. exps. in TM 1	18 Jun '16 (198)
(4) Mag. exps. in TM 1	14 Mar '17 (467)
(5) Decommissioning injections	04 Jul '17 (579)

fluctuations of the magnetic field on-board to then focus on the physical mechanisms describing these fluctuations for two different frequency regimes that we distinguish in our data.

### 3.2.1 Characterization of magnetic field fluctuations on-board

The fact that the four magnetometers of the magnetic diagnostics subsystem enclose the main instrument enables the direct comparison between different read-outs to disentangle spacecraft from interplanetary contributions. To do so, we use the coherence function which statistically quantifies common fluctuations between two time series. In the bottom right-hand panel of Fig. 3 we show the coherence function between the different channels of the magnetometers pair PX and PY, although the results shown are equivalent for each couple of magnetometers analysed. As shown in the figure, coherence between orthogonal axes is suppressed in the whole band while correlation between measurements on the same axes show a steep increase below 5 mHz. Given the low frequency of the coherent magnetic field fluctuations and the location of the magnetometers, these results point towards the interplanetary magnetic field fluctuations as the leading contribution in the sub-mHz frequency regime. On the other hand, fluctuations above the mHz region would be dominated by read-out electronics. This is further confirmed by the following analysis.

To evaluate the magnetic field and magnetic field gradient fluctuations we compute the amplitude spectral density (the square root of the power spectral density) by means of the Welch averaged periodogram (Welch 1967). We use data segments of 56 h and apply a Blackman–Harris window to prevent spectral leakage. To make sure that the window is not biasing our estimate we remove the lowest four frequency bins of the spectra. To compute the dots in the spectra we performed an averaging in the frequency domain, see the method described in the supplemental material of Armano et al. (2018b) for a further explanation. All the analysis and data post-processing were performed with LTPDA (Hewitson et al. 2009), a MATLAB toolbox designed for the analysis of the LPF data.

The spectra of magnetic field fluctuations are shown in the left-hand panel of Fig. 3, from top to bottom, for the X, Y, and Z components of the magnetic field, respectively. In this case, we notice that the two frequency regimes previously observed in the coherence function also appear with differentiated spectral behaviour above and below 5 mHz. Indeed, while the sub-mHz fluctuations show an almost constant spectral index, fluctuations above the mHz are flat and uncorrelated. Moreover, the magnitude of sub-mHz fluctuations is equal for all four magnetometers whereas in the high-frequency regime different magnetometers show a different noise plateau. In the different panels of Fig. 3 we show some fits to the data (the small dots). We will describe them in detail in Section 3.3, where we will show how changes in some parameters of the interplanetary media affect the spectrum of the magnetic field.

**Table 2.** Dates associated with events that impacted the magnetic environment on-board LPF. In parenthesis we include the DAL.

Event	Date (DAL)
(a) Coils check	11 Jan '16 (39)
(b) Propulsion module released	22 Jan '16 (50)
(c) DMU SW crash	5 May '16 (154)
(d) Cluster-2 DCIU anomaly	9 Jul '16 (219)
(e) LTP safe mode	24 Sep '16 (296)
(f) DMU SW crash and reboot	21 Oct '16 (296)
(g) Thruster-4 anomaly	27 Oct '16 (329)
(h) Cooling down	23 Jan '17 (417)
(i) Cooling down	29 Apr '17 (513)
(j) High-pressure latch valves switch	13 Jul '17 (588)

As we described in Section 2.2, not only the gradient of the magnetic field but also the fluctuations of this gradient can contribute as a force exerted on the test mass. Thus, we took advantage of the configuration of the magnetometers on-board to estimate the magnetic field gradient from the difference between magnetic field measurements on opposing sides of the LTP. Opposing magnetometers are separated by 0.65 cm in the PX-MX case, and 0.54 cm in the PY-MY case. Check bottom panel of Fig. 1 for a clear view of the set-up. All magnetometers in the spacecraft are placed in the same X–Y plane and, therefore, no estimates of the Z gradients were possible. In the right top and right middle panels of Fig. 3 we show the amplitude spectral density of the fluctuations of the magnetic field gradient across the X and Y axes, respectively, of LPF for the three components of the magnetic field. The spectra of the magnetic field gradient are flat at  $20 \text{ nT m}^{-1} \text{ Hz}^{-1/2}$  down to about 0.1 mHz, to even smaller frequencies than in the case of the magnetic field fluctuations. In this case, the noise measured seems to be in accordance with our electronics noise (see Section 3.2.3 for more details), and thus, we are limited by our instrument to measure any fluctuation smaller than this value. It should be reminded that this value is not likely to be representative of the magnetic field gradient at the test mass position, since any local source of magnetic field close to the test mass could be a potential source of magnetic field gradient that would not be measured by our pair of magnetometers if they are too far away from the mentioned source.

Although we have previously described the smooth shape of the magnetic field spectra, there are also some spectra lines appearing in the panels in Fig. 3. In some of them a line at 3.3 mHz appears in the PY magnetometer channels, with its corresponding harmonic at 10 mHz. Moreover, the signal appears to be stronger in the X component of the magnetic field. We cannot confirm the physical origin of these lines. However, since it is clearly visible in the magnetic field gradient across the Y-axis, this points out to a local origin and excludes any source coming from the interplanetary media, which would be sensed equally by all our magnetometers. The distribution of the units and the magnetometers on-board points towards the On-Board Computer (OBC) as the probable source of this magnetic field tone.

### 3.2.2 Fluctuations in the sub-millihertz: interplanetary magnetic field contribution

The interplanetary magnetic field measured by our magnetometers is imprinted on the solar wind plasma that surrounds the spacecraft and travels through the interplanetary media. Plasma fluctuations in interplanetary space have been successfully described in the

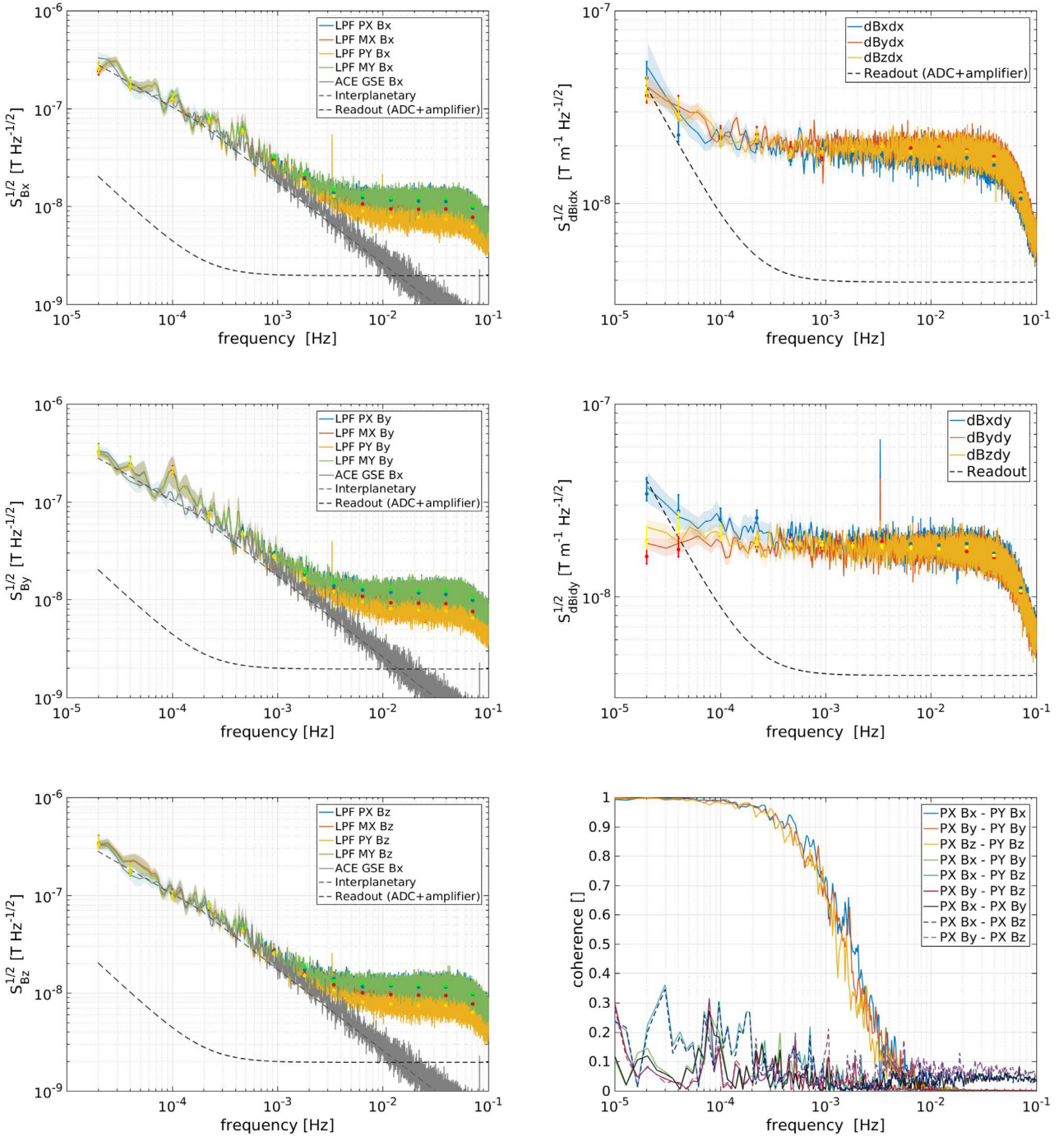


**Figure 3.** Characterization of the magnetic field environment on-board for the period from 2017 February 13 to March 2. *Left:* Spectrum of the, from top to bottom, X, Y, and Z components of the magnetic field from the four LPF magnetometers and from the ACE magnetometer. Dashed lines correspond to the contribution to LPF magnetometers coming from interplanetary magnetic field and electronics. *Right:* Spectrum of the gradient of the magnetic field along the X-axis (uppermost panel) and Y-axis (middle panel) on-board LPF. The dashed lines correspond to the contribution coming from electronics to LPF magnetometers. The bottom panel corresponds to the coherence function between the three axes magnetic field as measured in independent magnetometers on-board the satellite.

framework of the classical Kolmogorov turbulence (Kolmogorov 1941). In this framework, energy injected into the interplanetary plasma at large scales is transferred by non-linear interactions to microscales where it is finally dissipated, thus heating the plasma. The low-frequency part of the magnetic field and plasma-velocity

power spectra often exhibits a clear  $f^{-1}$  scaling, from DC up to frequencies of about  $10^{-4}$  Hz in the fast Alfvénic wind (Bruno et al. 2009), where the turbulent energy cascade becomes active. It is worth noting that, contrary to the fast solar wind, in the low-speed streams the injection range may cover a smaller range of

frequencies and sometimes not to be present at all (Bruno et al. 2019). At frequencies higher than  $10^{-4}$  Hz but below the ionic break that occurs around 0.1–1 Hz, we find what we call the inertial range. In this range, the solar wind is in a state of fully developed turbulence, where the magnetic energy spectrum has a well-defined Kolmogorov  $f^{-5/3}$  spectrum (Bruno & Carbone 2013). At frequencies higher than the ionic break the Kolmogorov spectrum breaks down and the magnetic fluctuations display a steeper  $f^{-7/3}$  power-law spectrum, up to frequencies of about 100 Hz (Sahraoui et al. 2009), where dissipation processes at proton scales take place. At even higher frequencies sometimes the spectrum steepens even more, roughly described by a further power law (Sahraoui et al. 2009) with a scaling exponent between  $f^{-3.5}$  and  $f^{-5.5}$ , or perhaps by an exponential decay (Alexandrova et al. 2012). Since these scales suffer for a lack of spacecraft measurements, a clear indication cannot be provided. This region of frequencies has been indicated as a range where collisionless dissipative mechanisms are efficiently at work at electron scales (Sahraoui et al. 2009) & (Alexandrova et al. 2012) & (Goldstein et al. 2015).

In order to check our measurements with previous characterization of the solar wind, in the left-hand panels of Fig. 3 we compare the amplitude spectral density of magnetic field fluctuations obtained during a LPF noise run to a set of data obtained from the Advanced Compton Explorer (ACE) (Smith et al. 1998) in the same period of time. The ACE mission monitors different parameters of the solar wind by means of a suite of instruments on-board and, as LPF, follows a Lissajous orbit around L1. It is therefore a useful data set with which to compare our measurements. ACE data is shown in Geocentric Solar Ecliptic Coordinates (GSE) system, which has its  $X$ -axis pointing from Earth towards the Sun and its  $Y$ -axis is chosen to be in the ecliptic plane pointing towards dusk. It is worth mentioning that even though both satellites are orbiting around L1, the distance separating them can be of the order of  $10^5$ – $10^6$  km. However, we can safely compare the fluctuations of the magnetic field between both satellites at frequencies around the 20–50  $\mu$ Hz, which is the band in which we will focus our analysis. As we will discuss in more detail, the typical velocity of around 200–500 km  $s^{-1}$  of the solar wind guarantees that fluctuations in this frequency range have a coherence length greater than the distance between both spacecraft.

Our results show that, for frequencies below 3 mHz, the amplitude of fluctuations measured in LPF are in agreement with those measured by ACE during the same period of time. The spectral index obtained by both instruments is in agreement with previous characterizations of the spectra of interplanetary magnetic field fluctuations corresponding to the inertial range, as we will see in detail in Section 3.3. From our analysis we confirm that whilst the absolute value of the magnetic field on-board is dominated by the units inside the spacecraft, the fluctuations of the magnetic field are instead dominated by the fluctuations of the interplanetary magnetic field. At the same time, this corroborates the results obtained in the bottom right-hand panel of Fig. 3. Since all magnetometers are measuring the interplanetary contribution, fluctuations of the magnetic field are completely correlated in the low-frequency range for those channels measuring the magnetic field in a given direction. This correlation decays if we compare measurements of the magnetic field in transverse directions. As expected, the correlation between fluctuations of the magnetic field disappears for frequencies above 3 mHz. As we show in the following, this frequency range is dominated by electronic noise, i.e. with no common correlation between channels.

### 3.2.3 Fluctuations above the millihertz: fluxgate read-out electronics

In Section 2.2 we provided a description of the read-out chain of the magnetometers. The noise analysis for this chain shows that the amplifier and the analogue-to-digital converter which will limit the performance of our sensor at low and high frequencies, respectively. If we take into account the different components in the read-out chain and the noise figures in the data sheet values, we obtain the contribution shown in the different panels of Fig. 3. On the one hand, in the low-frequency region, the noise follows a  $f^{-1}$  spectrum produced by the instrumentation amplifier. On the other hand, in the high-frequency region, the spectrum is flat due to the analogue-to-digital converter which sets a limit of  $S_{ADC}^{1/2} \simeq 2$  nT  $Hz^{-1/2}$  at the high-frequency band. In the left-hand panels of Fig. 3 we show, for the three different axes, the noise floor measured by the four magnetometers on-board during the period. On-board magnetometers measured a noise level above 3 mHz that differs for each magnetometer in a range that goes from 7 nT  $Hz^{-1/2}$  in the PY magnetometer to 11 nT  $Hz^{-1/2}$  in the MY magnetometer, all of them above the expected 2 nT  $Hz^{-1/2}$ . Considering that the amplitude of the interplanetary fluctuations decay as  $f^{-1.65}$  and taking into account that the observed noise is not correlated between the four magnetometers – see bottom right-hand panel of Fig. 3, we conclude that the read-out electronics must be the source of this excess noise. We have investigated this by focusing on the electronics design of the magnetometer read-out. Our analysis shows that this noise contribution could be assigned to a common-mode noise at the input of the instrumentation amplifier, which can be originated due to the lack of common ground between magnetometer and electronics read-out. We have experimentally tested this hypothesis by means of an engineering model of the LISA Pathfinder Data Management Unit (DMU) (Canizares et al. 2011), which included the Data Acquisition Unit (DAU) unit together with a flight model fluxgate magnetometer. With this set-up we have verified that the measured noise plateau can vary from the design 2 nT  $Hz^{-1/2}$  if both units are not commonly grounded. Hence, we conclude that the observed excess noise above 3 mHz could be assigned to this issue. Although it is not possible to assess the exact contribution to the noise budget due to this effect, a worst-case estimate sets a value of 90 mV  $Hz^{-1/2}$  for the required fluctuations at the input of the instrumentation amplifier in order to explain the excess observed by our magnetometers. This value is relatively high compared to our read-out voltage noise. Since it is not possible to measure the common-mode noise at the spacecraft, we are only establishing an upper bound without discarding other possible contributions to the excess noise in the high-frequency band. It is important to stress here that the main objective of the magnetometers on-board LPF was to track slowly varying magnetic fields that are the ones that can have an impact in the dynamics of the free-falling test mass. Hence, an excess noise in the high-frequency range, though unexpected, does not have an impact on the scientific objectives of the magnetic diagnostic subsystem, but if needed, it could be corrected for a future space-based gravitational wave mission.

### 3.3 Non-stationarities in the magnetic field fluctuations

Until now we have based our analysis on the amplitude spectral density, which entails the information of the magnetic field in the frequency span of interest. The amplitude spectral density effectively describes the fluctuations during a fixed period of time. Hence, it would only be a complete statistical description if the

environment on-board LPF were stationary. This is obviously not the case. On the contrary, several situations can induce abrupt changes in the measured magnetic field. In Table 2 we provided a series of events that we identified in the magnetic field timeline. Since these were associated to satellite operations these events are both easily identified and, eventually, removed from the data set through post-processing. A second, more complex, class of non-stationarity is the one associated to the interplanetary magnetic field. In Section 3.2.2 we described the origin of the spectral index of the observed magnetic field fluctuations in the low-frequency range and its relation with the solar wind speed. A rich variety of interplanetary structures is superposed to the unperturbed solar wind plasma (Kilpua, Koskinen & Pulkkinen 2017) & (Richardson 2018). Structures such as corotating interaction regions, interplanetary shocks, magnetic clouds or heliospheric current sheet crossings will induce variations in the measured magnetic field on-board the spacecraft.

Since our DC magnetic field is completely dominated by the spacecraft components: around  $\sim 1\mu\text{T}$ , compared with the  $\sim 1\text{nT}$  coming from the interplanetary media, we cannot measure the absolute value of the interplanetary magnetic field in these cases. Nevertheless, if the variations are strong enough (of the order of  $\sim 10\text{nT}$ , for example) and especially if we see them in all four magnetometers, we could indeed assign an interplanetary origin to them. Accurate detection of the magnetic imprint of these events requires the magnetometers to be isolated from spacecraft contributions. This is the case for dedicated space weather mission which place the magnetometers at the end of a deployable boom, such as in the case of ACE (Smith et al. 1998) or WIND (Lepping et al. 1995) missions. Moreover, these missions contain a suite of instruments that allow a complete characterization of the plasma, tracking parameters such as the solar wind speed or the number density of the plasma that we will refer in the following. Nonetheless, it is worth noticing that, although not designed for that, the radiation monitor on-board LPF (Canizares et al. 2011; Armano et al. 2018a) allowed for the detection of the passage of large-scale interplanetary structures such as high-speed solar wind streams and interplanetary counterparts of coronal mass ejections generating recurrent and non recurrent depressions of the Galactic cosmic ray flux (Armano et al. 2018c, 2019c).

As we have previously discussed, in LPF the effect of the interplanetary magnetic field structures cannot be easily distinguished in the absolute value of the measured magnetic field because the local magnetic field is largely dominated by the contribution of the spacecraft units. However, as we show in the following, the effect of these structures can have an impact in the spectra of fluctuations in the low-frequency band, i.e. below the Hz.

In order to trace the variability of the spectrum we took a closer look at the amplitude of the spectra in two different frequency regions, namely  $20\ \mu\text{Hz} < f_{LF} < 50\ \mu\text{Hz}$  and  $20\ \text{mHz} < f_{HF} < 40\ \text{mHz}$ . We selected these two frequency regions because, as discussed above, magnetic field fluctuations come from a different physical origin, i.e. interplanetary magnetic field and magnetometer read-out electronics, respectively. For each of these frequency windows we compute the power spectral density. We selected windows of 16 h to compute each bin. In order to avoid segments containing magnetic experiments or events as the ones reported in Tables 2 and 1, we apply a mask to the data. To do so we take as a figure of merit the amplitude spectral density in the range  $1\ \text{mHz} < f < 10\ \text{mHz}$ . Those segments where this figure of merit is exceeded by five sigma are discarded from our analysis. Following this criterion, we exclude 9 segments out of 300. This analysis allows

a generic description of the statistical behaviour of the fluctuations without any previous assumption on its stationarity. Fig. 4 shows the results for both frequency ranges. In agreement with our previous analysis, the amplitude of the fluctuations for the low-frequency bin is coherent and follows the same statistical distribution for all four magnetometers. Bins are statistically distributed with similar median values, namely

$$\tilde{S}_{B_z, PY}^{1/2} \Big|_{f_{LF}} = 177_{-53}^{+80} \text{ nT Hz}^{-1/2},$$

$$\tilde{S}_{B_z, MY}^{1/2} \Big|_{f_{LF}} = 182_{-60}^{+81} \text{ nT Hz}^{-1/2},$$

$$\tilde{S}_{B_z, PX}^{1/2} \Big|_{f_{LF}} = 191_{-62}^{+101} \text{ nT Hz}^{-1/2},$$

$$\tilde{S}_{B_z, MX}^{1/2} \Big|_{f_{LF}} = 189_{-64}^{+102} \text{ nT Hz}^{-1/2}.$$

These values are based on the 16th, 50th, and 84th percentiles of the histogram. Also, in this case we can derive a common mean value for the fluctuations in this frequency range of  $207 \pm 6\ \text{nT Hz}^{-1/2}$ . On the other hand, the noise power in the higher frequency bins show a different amplitude spectral density for each magnetometer. The median values in this case are

$$\tilde{S}_{B_z, PY}^{1/2} \Big|_{f_{HF}} = 7.4_{-0.3}^{+0.8} \text{ nT Hz}^{-1/2},$$

$$\tilde{S}_{B_z, MY}^{1/2} \Big|_{f_{HF}} = 12.3_{-0.7}^{+2} \text{ nT Hz}^{-1/2},$$

$$\tilde{S}_{B_z, PX}^{1/2} \Big|_{f_{HF}} = 10.6_{-0.6}^{+2} \text{ nT Hz}^{-1/2},$$

$$\tilde{S}_{B_z, MX}^{1/2} \Big|_{f_{HF}} = 9.0_{-0.6}^{+0.8} \text{ nT Hz}^{-1/2}.$$

In the latter we observe that the distribution of the median values is narrower and not overlapping between them. Both behaviours are clearly distinguished in the histograms of Fig. 4, which characterizes the variability of the magnetic field fluctuations on-board for the two frequency regimes that we have previously identified.

In the framework of future gravitational wave detectors in space, the variability in the spectra of magnetic field fluctuations is particularly relevant in the low-frequency regime. There are two main reasons for that: first, the mHz band is the main objective of a gravitational wave detector in space, since these observatories are designed to study the gravitational wave universe in this frequency band. Second, at the same time, the low-frequency fluctuations will be precisely the main contribution to the magnetic induced force noise in the free-falling test masses. According to Armano et al. (2016), magnetic induced forces could contribute to a maximum of  $3\ \text{fm s}^{-2} \text{ Hz}^{-1/2}$  of the measured  $12\ \text{fm s}^{-2} \text{ Hz}^{-1/2}$  at  $0.1\ \text{mHz}$  of the differential acceleration measured on LPF test masses. Although the precise determination of the magnetic noise contribution is still pending, the current estimate is expected to be of the order of other contributions such as the charging noise, with an expected contribution of  $1\ \text{fm s}^{-2} \text{ Hz}^{-1/2}$  (Armano et al. 2017) or the actuation noise, which is expected to be the dominant contribution with an expected value of  $4.5\ \text{fm s}^{-2} \text{ Hz}^{-1/2}$  (Armano et al. 2016) at  $0.1\ \text{mHz}$ . For that reason it is worth characterizing further the variability in this frequency regime to provide information for future spaceborne observatories. As we show in the following, the fluctuations of the magnetic field in the sub-mHz band are deeply connected to the dynamics of the interplanetary plasma.

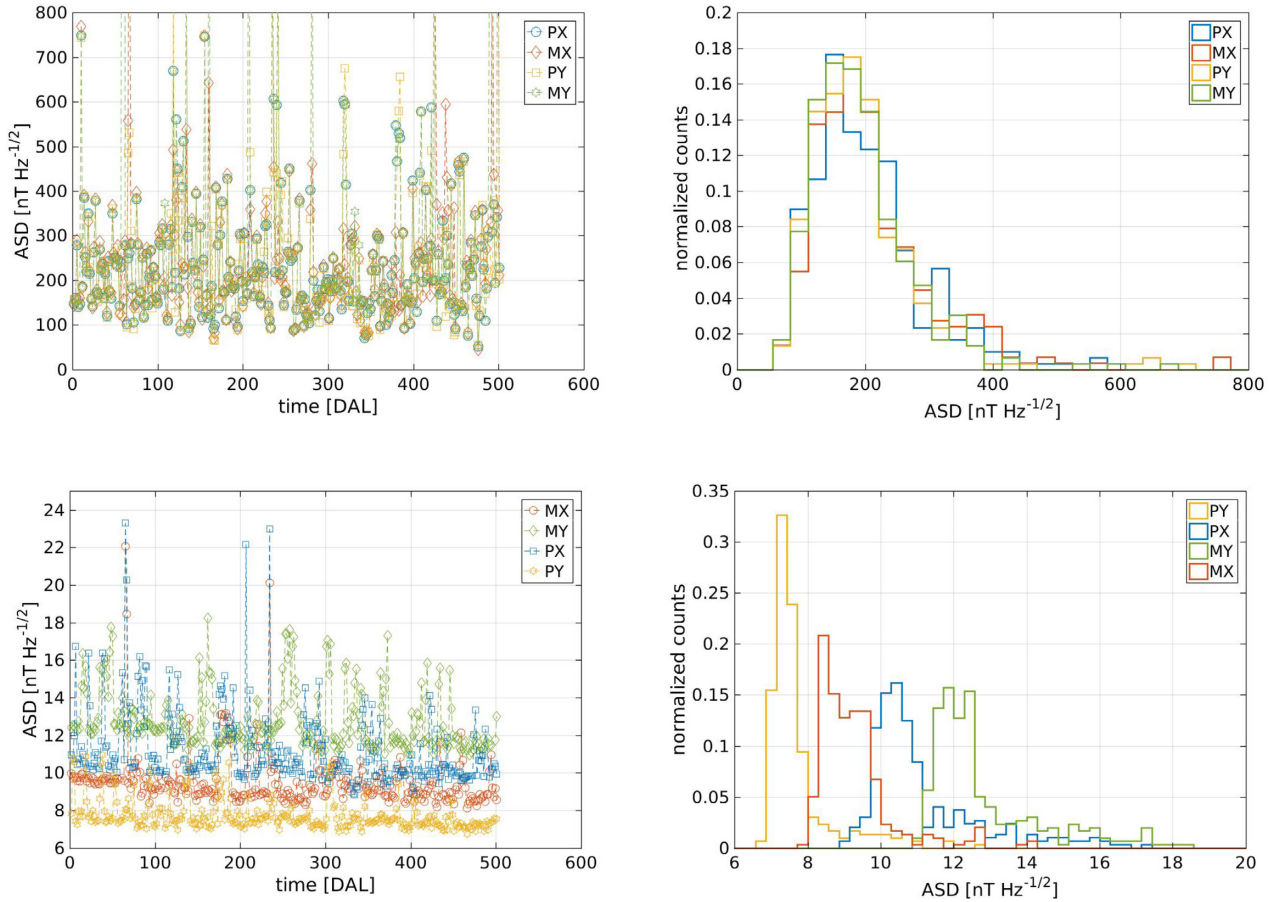


**Figure 4.** Time evolution and statistical distribution of the X-component of the magnetic field fluctuations as measured on-board, for two different frequency regimes. Colours correspond to magnetometers: PX (blue), MX (red), PY (yellow), and MY (green). Time is indicated in DAL, while ASD stands for Amplitude Spectral Density. *Top*: Fluctuations in the frequency range  $20 < f < 50 \mu\text{Hz}$ . *Bottom*: Fluctuations in the frequency range  $20 < f < 40 \text{mHz}$ .

Fluctuations in the intensity of the interplanetary magnetic field can be associated with a wide variety of phenomena (Bruno & Carbone 2013). However, particularly in the inertial range, the amplitude of the magnetic fluctuations is strictly related to their Alfvénic nature. The solar wind is highly structured in high- and low-speed streams, which carry different types of fluctuations. While fast wind is characterized by large-amplitude Alfvénic fluctuations, the slow wind generally advects less Alfvénic fluctuations characterized by a smaller amplitude, with the important exception of the Alfvénic slow wind (see D’Amicis & Bruno 2015). This means that, moving from high- to low-speed regions, the power level of the magnetic fluctuations within the inertial range progressively decreases, though keeping the typical  $f^{-5/3}$  Kolmogorov scaling. As a matter of fact, solar wind turbulence may be thought as superposition of a magnetic field background spectrum, common to both fast and slow flows (Bruno et al. 2017), and a turbulent large-amplitude Alfvénic spectrum, characteristic of the fast solar wind.

In order to study the impact of the solar wind speed in our measurements, we selected three segments representing stable periods of solar wind speed. These periods had to be long enough to allow an estimate of amplitude spectral density down to  $20 \mu\text{Hz}$ . The selected time spans correspond to 2016 July 7–14, 2017 May 28–June 1, and 2017 February 11–16 when, according to measurements recorded by ACE, the solar wind had a mean velocity of  $553 \pm 47 \text{ km s}^{-1}$ ,  $390 \pm 53 \text{ km s}^{-1}$  and  $335 \pm 35 \text{ km s}^{-1}$ , respectively. For each of

these segments we evaluated the amplitude spectral density of the magnetic field as measured by LPF magnetometers. Although other authors have already studied this phenomena (Bruno et al. 2017), we extended the characterization to the sub-mHz regime, which is the region of greatest interest for LISA and future gravitational wave detectors.

Results are shown in Fig. 5, where we can distinguish an increase in the power of the low-frequency fluctuations that correlates with the increase of solar wind velocity. Indeed, we observe that fluctuations at  $20 \mu\text{Hz}$  vary from  $170_{-10}^{+30} \text{ nT Hz}^{-1/2}$  for a slow wind situation (typical velocities  $v \simeq 300 \text{ km s}^{-1}$ ) to  $750_{-50}^{+100} \text{ nT Hz}^{-1/2}$  when we consider a situation of high-speed wind (typical velocities  $v \simeq 500 \text{ km s}^{-1}$ ). These two scenarios represent a deviation of 18 and 362 per cent, respectively, with respect to the mean value that we have previously derived for the complete time series,  $207 \pm 6 \text{ nT Hz}^{-1/2}$ . Although other phenomena may also contribute to the variability of the sub-mHz fluctuations of the spectra, we consider this correlation with the solar wind as one of the physical mechanisms behind the statistical distribution of the fluctuations in the sub-mHz band that we obtained in Fig. 4. It is thus a dependence that future space-borne gravitational wave detectors will need to take into account, since as we mentioned in Section 2.1, the coupling of the magnetic field fluctuations with the magnetic moment of the test masses could produce spurious forces that a gravitational wave detector would sense as a change in the acceleration noise, and therefore, possibly mistaking it as a gravitational wave signal.

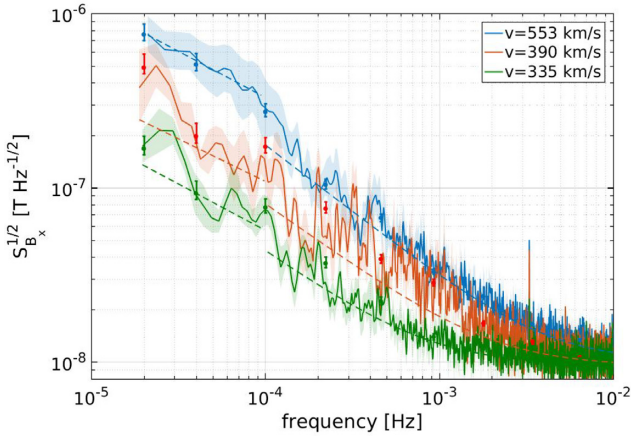


**Figure 5.** Amplitude spectral density of the X-component of the magnetic field for three periods of different solar wind speed. The data to compute each spectrum has been obtained combining the data from the four magnetometers. The values of the fits to the data (dashed lines) are reported in Table 3.

In Table 3 we characterize the variation of the shape of the magnetic field fluctuations in terms of the solar wind speed. We fitted the spectra of the magnetic field fluctuations to two power laws, one between 20–100  $\mu\text{Hz}$  and another one from 100  $\mu\text{Hz}$  to 10 mHz. We have made this differentiation because, as previously explained, different mechanisms act at different time-scales, resulting in different spectral indexes for these power laws. The fits were performed by means of a chi-squared minimization, non-linear fit using derivative-free method. For the sake of completeness, in Table 3 we also show the results of the analysis for the  $Y$  and  $Z$  axes, which are not shown in the figure.

It is interesting to notice that, according to our parametrization, the main impact of the wind speed is in the parameter  $B$  which accounts for the power of the fluctuations in the frequency band described by the power law. The values for the spectral index  $C$  are around 1.5, smaller than the value expected, which is 1.65, for the inertial range of interplanetary magnetic field fluctuations. This small difference may come from the fact that in the LPF case, the read-out noise of the magnetometers starts to flatten the spectrum around 1 mHz, and this may result in a slightly less steep curve when we perform the fit. Moreover, the inertial range of interplanetary magnetic field fluctuations starts between 0.1–1 mHz, while the magnetometers read-out noise starts to be dominant around 1 mHz. Therefore, we cannot see a large and clear portion of the inertial range part of the interplanetary magnetic field spectrum. With regard to the parameter  $A$ , the comparison between the different wind velocity regimes do not show any significant variation, as we expected given that this parameter describes the noise floor of the instrument, which is dominated by the electronics read-out contribution. When we analyse the parameters corresponding to the lower frequency part, we find that the spectral index  $E$  values are around 1, which are in good agreement with the  $f^{-1}$  behaviour of the interplanetary magnetic field fluctuations at this frequency range – even though the errors are high because we do not have many points for the fit. Finally, the values obtained for the parameter  $D$  are not very well fitted, probably because of the small amount of data points available in this frequency range.

To finalize the study of the non-stationarity of the magnetic field fluctuations, we took a closer look at the impact of this contribution during the noise performance runs. Analogously as it is done with

**Table 3.** Values of the fits of the dashed lines shown in Fig. 5 to a function  $A + B 2\pi f^{-C}$  in the range 100  $\mu\text{Hz}$  – 10 mHz and to a function  $D 2\pi f^{-E}$  in the range 20  $\mu\text{Hz}$  – 100  $\mu\text{Hz}$ .

Parameter	Solar wind speed [ $\text{km s}^{-1}$ ]		
	553 $\pm$ 47	390 $\pm$ 53	335 $\pm$ 35
$B_x$			
A ( $10^{-16} \times [\text{T}^2/\text{Hz}]$ )	1.02 $\pm$ 0.03	0.90 $\pm$ 0.02	0.91 $\pm$ 0.02
B ( $10^{-19} \times [\text{T}^2/\text{Hz}]$ )	3.8 $\pm$ 0.6	1.8 $\pm$ 0.4	0.6 $\pm$ 0.2
C [ ]	1.53 $\pm$ 0.03	1.42 $\pm$ 0.04	1.41 $\pm$ 0.06
D ( $10^{-17} \times [\text{T}^2/\text{Hz}]$ )	4 $\pm$ 10	1 $\pm$ 30	0.1 $\pm$ 0.4
E [ ]	1.1 $\pm$ 0.3	1.0 $\pm$ 0.5	1.0 $\pm$ 0.4
$B_y$			
A ( $10^{-16} \times [\text{T}^2/\text{Hz}]$ )	1.11 $\pm$ 0.03	0.86 $\pm$ 0.02	0.94 $\pm$ 0.02
B ( $10^{-19} \times [\text{T}^2/\text{Hz}]$ )	2.8 $\pm$ 0.4	1.9 $\pm$ 0.6	0.3 $\pm$ 0.1
C [ ]	1.58 $\pm$ 0.03	1.34 $\pm$ 0.06	1.53 $\pm$ 0.07
D ( $10^{-17} \times [\text{T}^2/\text{Hz}]$ )	6 $\pm$ 20	0.001 $\pm$ 0.006	2 $\pm$ 10
E [ ]	1.0 $\pm$ 0.3	1.7 $\pm$ 0.4	0.8 $\pm$ 0.5
$B_z$			
A ( $10^{-16} \times [\text{T}^2/\text{Hz}]$ )	1.09 $\pm$ 0.02	0.91 $\pm$ 0.02	0.96 $\pm$ 0.01
B ( $10^{-19} \times [\text{T}^2/\text{Hz}]$ )	1.2 $\pm$ 0.2	1.0 $\pm$ 0.3	0.22 $\pm$ 0.08
C [ ]	1.62 $\pm$ 0.03	1.46 $\pm$ 0.05	1.60 $\pm$ 0.06
D ( $10^{-17} \times [\text{T}^2/\text{Hz}]$ )	0.3 $\pm$ 0.9	10 $\pm$ 20	0.000 $\pm$ 0.001
E [ ]	1.3 $\pm$ 0.3	0.6 $\pm$ 0.1	1.8 $\pm$ 0.4

on-ground gravitational wave detectors during science runs, in LPF these runs were periods where the instrument was configured in its more sensitive configuration and kept in data acquisition mode without introducing any calibration signal. For LISA Pathfinder, these noise performance runs took typically 5 to 10 days although it is worth stressing that future space-borne gravitational wave detectors, such as LISA, aim to spend weeks or months in this scientific acquisition mode.

In Fig. 6 we analysed the non-stationarities of the low-frequency part of the magnetic field spectrum during the two LPF noise runs that were published in Armano et al. (2016) (2016 April noise run) and Armano et al. (2018b) (2017 February noise run). Following the same approach as we have previously shown, we computed the amplitude spectral density of the magnetic field in the frequency span that goes from 20–50  $\mu\text{Hz}$ . In the top panels of Fig. 6 we show the evolution of this value over the duration of each LPF noise run for LPF and ACE satellites. We compare this with the evolution of the time series of the magnetic field itself  $B_x$  component in Global Solar Ecliptic (GSE) coordinates (second panel) for ACE. In the same panel, we also show the magnetic field  $B_z$  component as measured in LPF during the same period. The reason to compare LPF's  $B_z$  in LPF reference frame with ACE's  $B_x$  in GSE coordinates is that LPF's  $Z$ -axis points always towards the solar panel, which is always pointing towards the Sun. Thus, LPF positive  $Z$ -axis is roughly equivalent to positive  $X$ -axis in GSE coordinates. To do this comparison, LPF data has been low-pass filtered at 1 mHz in order to remove the higher frequency noise coming from electronics and the mean subtracted in order to exclude the DC magnetic field coming from the spacecraft components. As we previously showed when analysing the components in the spectra, the main features of the long term evolution are driven by the interplanetary component. As we saw, the phenomena associated with the solar wind requires several parameters that detail the characteristics of the interplanetary plasma. In order to provide a comprehensive view of this phenomena during these two particular noise runs we show as well the solar wind speed (third panel) and the proton density (fourth panel), as measured by ACE.

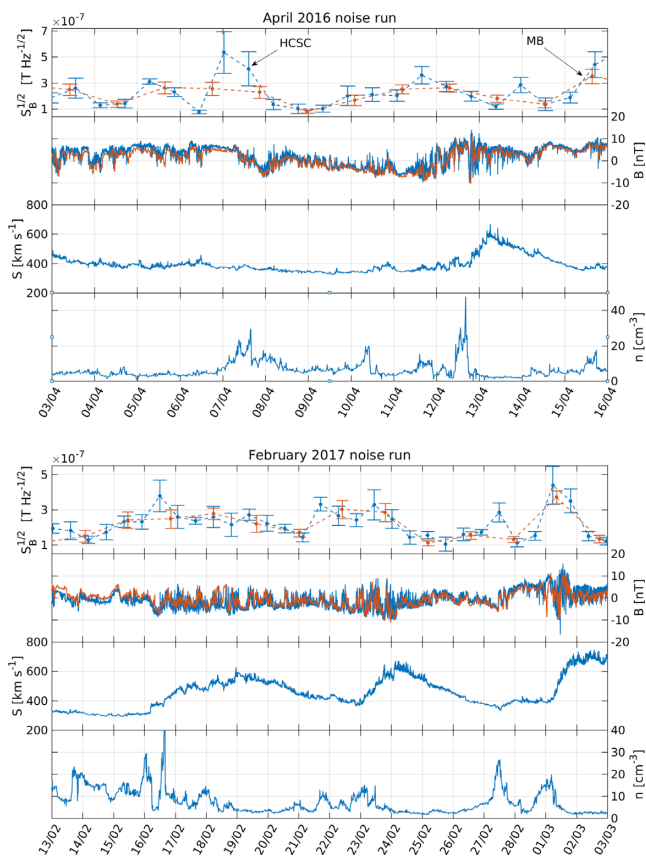


**Figure 6.** *Top:* Evolution during 2016 April noise run in LPF (dates indicated in figure) from (top to bottom): *Upper Top:* Noise power in the 20–50  $\mu\text{Hz}$  frequency bin for an average of the three components of LPF PY magnetometer (red) and ACE magnetometer (blue). The events listed are taken from Armano et al. (2019c) and noted in the text. *Middle top:* Magnetic field  $B_x$  component in GSE coordinates measured by ACE (blue), and LPF PY magnetometer  $B_x$  component (red) with a lowpass at 1 mHz and with its mean value subtracted. *Middle bottom:* Solar wind velocity in GSE coordinates as measured by ACE. *Lower bottom:* Proton density measured by ACE. *Bottom:* Same as top figure but for the 2017 February noise run performed in LPF (dates indicated in figure).

The results show that, during the 2017 February noise run, there are roughly three clear increases in the ASD of the low-frequency bin of the magnetic field. These three peaks seem to be caused by high-speed streams in the solar wind speed, i.e. sudden increases in the solar wind speed, a type of event that also carries a decrease in the proton density, as we can also clearly observe in the lowest panel. Regarding the 2016 April noise run, we can see another high-speed stream around April 13th that causes another small peak in the ASD of the low-frequency bin of the magnetic field, associated with the corresponding decrease in proton density. Apart from that, there are two events that cause another increase in the time series of the first panel. According to Armano et al. (2019c), these events would be associated to a Heliospheric current Sheet Crossing (HCSC) and a Magnetic Barrier (MB). We refer the reader to the aforementioned reference for more details on these events.

#### 4 CONCLUSIONS

In this work we provide for the first time a description of the magnetic field on-board a gravitational wave detector technology demonstrator in space. Our characterization is tailored to address

challenges created by the magnetic field that space-borne gravitational wave observatories will face when they become operative.

LPF included four magnetometers as part of its magnetic diagnostic subsystem. They were placed inside the thermal shield surrounding the optical bench and the vacuum chambers containing the test masses. Due to the magnetic content of the fluxgate core, the magnetometers had to be placed far enough from the test masses to prevent this active magnetic core to induce magnetic forces on the free-falling test masses. The major drawback of this configuration is the lack of resolution to measure the magnetic field or the magnetic field gradient at the location of the test masses.

The DC magnetic field measured on-board is completely dominated by the contribution from the electronics of the spacecraft units. Among them, the thruster systems were a major contributor, both the cold gas high-pressure latch valves (the ones used by ESA) and the colloidal thrusters (the ones operated by NASA). Cold gas thrusters or, more precisely, some permanent magnets in the cold gas thruster subsystem, contribute with roughly the 80 per cent of the measured magnetic field. Although a strong contribution, this one remains constant throughout the mission – partially thanks to the high thermal stability reached on-board (Armano et al. 2019b) – which is key for a mission as LISA with strong requirements on any potential source of fluctuations. This is not the case for the colloidal thrusters, where we observed a persistent slow drift of around 150 nT for the measurement of two magnetometers close to the test masses. This 150 nT drift took place over around 150 days, which corresponds to the first period of DRS operations – see Fig. 2 to check the different periods. We attribute this effect to the displacement of a stainless steel bellow inside the thruster that keeps the propellant at a constant pressure. Although not a desirable effect for future gravitational wave detectors in space, this slow change in the local magnetic field should not be present in future missions, since it could impact the main measurement of a mission like LISA.

We took special care on the analysis of the fluctuations of the magnetic field on-board since these are a key component of the test mass force noise apportioning. We report how, on the one hand, the fluctuations of the magnetic field on-board are dominated at frequencies above the mHz by the contribution of the read-out electronics. In this frequency regime we identified and characterized an excess noise when compared to the design curve of our electronics. Although unexpected, this does not represent a major problem since the frequencies in which the magnetic noise may have an important impact are below the mHz. On the other hand, below the mHz, the fluctuations are dominated by the contribution from the interplanetary magnetic field. Several indications point toward an interplanetary origin of the low-frequency fluctuations of the magnetic field. First, all magnetometers show coherent fluctuations in this frequency regime and, second, the densities of the magnetic field components measured by our four magnetometers match those measured by dedicated space weather missions ACE and WIND, which are also orbiting around L1.

Finally, we evaluated the non-stationary component affecting the very low-frequency regime of the magnetic field fluctuations. Due to its dependence with the solar wind, the low-frequency fluctuations show a large variability associated with changes in the interplanetary plasma. We tracked the amplitude spectral density in the low end of the LISA measuring band, i.e. at 20  $\mu\text{Hz}$ , during the whole duration of the mission. In this frequency regime, the magnetic field fluctuation on-board has a typical mean value of  $207 \pm 6 \text{ nT Hz}^{-1/2}$ , although it shows an important variability with a wide statistical distribution of its values. Following previous studies, we show how this variability is tightly associated with a variety of phenomena

associated with the dynamics of the interplanetary plasma. We have described and characterized how quantities describing the solar wind, as for example the plasma velocity, can be used to parametrize the variability of the low-frequency fluctuations. In the case of the solar wind velocity, we saw how variations in the range of 300–500 km s<sup>-1</sup> are related to variations in the amplitude spectral density in the range 20 – 50 μHz of around 170 – 750 nT Hz<sup>-1/2</sup>. We want to stress that the variability of the spectra in this low-frequency regime is particularly relevant for LISA since these are frequencies in the measurement band of LISA and, also, where the magnetic fluctuations are important to the noise budget, as they are proportional to induced force noise in the test mass. Hence, variabilities of the order of 300 per cent in the spectra of magnetic field fluctuations (as the ones reported here) have to be taken into account in the design phase in order to prevent that this non-stationary behaviour impacts the performance of the future observatory.

Having an instrument performance curve that is independent of the changes of the environment has been, historically, one of the main efforts of the gravitational wave community. By using the data of a pioneer mission (as LPF was) we expect to contribute to this decade-long effort but now putting the focus on the interplanetary environment. We consider that our description and analysis on the magnetic field on-board and its associated potential sources of fluctuations will help the design of future long-term gravitational wave observatories in space, like LISA will be.

## ACKNOWLEDGEMENTS

This work has been made possible by the LISA Pathfinder mission, which is part of the space science program of the European Space Agency. The French contribution has been supported by CNES (Accord Specific de projet CNES 1316634/CNRS 103747), the CNRS, the Observatoire de Paris, and the University Paris Diderot. EP and HI would also like to acknowledge the financial support of the UnivEarthS Labex program at Sorbonne Paris Cité (ANR-10-LABX-0023 and ANR-11-IDEX-0005-02). The Albert-Einstein-Institut acknowledges the support of the German Space Agency, DLR. The work is supported by the Federal Ministry for Economic Affairs and Energy based on a resolution of the German Bundestag (FKZ 500Q0501 and FKZ 500Q1601). The Italian contribution has been supported by Agenzia Spaziale Italiana and Istituto Nazionale di Fisica Nucleare. The Spanish contribution has been supported by Contract Nos. AYA2010-15709 (MICINN), ESP2013-47637-P, and ESP2015-67234-P (MINECO). MN acknowledges support from Fundación General CSIC (Programa ComFuturo). FR acknowledges support from a Formación de Personal Investigador (MINECO) contract. The Swiss contribution acknowledges the support of the Swiss Space Office (SSO) via the PRODEX Programme of ESA. LF acknowledges the support of the Swiss National Science Foundation. The UK groups wish to acknowledge support from the United Kingdom Space Agency (UKSA), the University of Glasgow, the University of Birmingham, Imperial College, and the Scottish Universities Physics Alliance (SUPA). JIT and JS acknowledge the support of the U.S. National Aeronautics and Space Administration (NASA).

## REFERENCES

- Alexandrova O., Lacombe C., Mangeny A., Grappin R., Maksimovic M., 2012, *ApJ*, 760, 121
- Amaro-Seoane P. et al., 2017, preprint(arXiv:eprint)
- Antonucci F. et al., 2012, *Class. Quant. Grav.*, 29, 124014
- Anza S. et al., 2005, *Class. Quant. Grav.*, 22, S125
- Armano M. et al., 2015, *J. Phys.: Conf. Ser.*, 610, 012024
- Armano M. et al., 2016, *Phys. Rev. Lett.*, 116, 231101
- Armano M. et al., 2017, *Phys. Rev. Lett.*, 118, 171101
- Armano M. et al., 2018a, *Astropart. Phys.*, 98, 28
- Armano M. et al., 2018b, *Phys. Rev. Lett.*, 120, 061101
- Armano M. et al., 2018c, *ApJ*, 854, 113
- Armano M. et al., 2019a, *Phys. Rev. D*, 99, 122003
- Armano M. et al., 2019b, *MNRAS*, 486, 3368
- Armano M. et al., 2019c, *ApJ*, 874, 167
- Bruno R., Carbone V., 2013, *Living Rev. Sol. Phys.*, 10, 2
- Bruno R. et al., 2009, *Earth Moon Planets*, 104, 101
- Bruno R., Telloni D., DeLure D., Pietropaolo E., 2017, *MNRAS*, 472, 1052
- Bruno R., Telloni D., Sorriso-Valvo L., Marino R., De Marco R., D’Amicis R., 2019 627, A96
- Canizares P. et al., 2009, *Class. Quant. Grav.*, 26, 094005
- Canizares P. et al., 2011, *Class. Quant. Gravi.*, 28, 094004
- D’Amicis R., Bruno R., 2015, *ApJ*, 805, 84
- Diaz-Aguilo M., García-Berro E., Lobo A., 2012, *Phys. Rev. D*, 85, 042004
- Diaz-Aguiló M., Mateos I., Ramos-Castro J., Lobo A., García-Berro E., 2013, *Aerosp. Sci. Technol.*, 26, 53
- Goldstein M., Wicks R., Perri S., Sahraoui F., 2015, *Phil. Trans. R. Soc. A*, 373, 20140147
- Hewitson M. et al., 2009, *Class. Quant. Grav.*, 26, 094003
- Kolmogorov A. N., 1941, *Cr Acad. Sci. URSS*, 30, 301
- Kilpua E., Koskinen H. E., Pulkkinen T. I., 2017, *Living Rev. Sol. Phys.*, 14, 5
- Lepping R. et al., 1995, *Space Sci. Rev.*, 71, 207
- Richardson I. G., 2018, *Living Rev. Sol. Phys.*, 15, 1
- Sahraoui F., Goldstein M., Robert P., Khotyaintsev Y. V., 2009, *Phys. Rev. Lett.*, 102, 231102
- Sanjuán J., Lobo A., Nofrarias M., Ramos-Castro J., Riu P. J., 2007, *Rev. Sci. Instrum.*, 78, 104904
- Sanjuan J., Lobo A., Nofrarias M., Ramos-Castro J., Mateos N., Xirgu X., 2009, *J. Phys.: Conf. Ser.*, 154, 012001
- Smith C. W., L’Heureux J., Ness N. F., Acuna M. H., Burlaga L. F., Scheifele J., 1998, *Space Sci. Rev.*, 86, 613
- Welch P., 1967, *IEEE Trans. Audio Electroacoust.*, 15, 70
- Ziemer J. K. et al., 2006, *AIP Conf. Proc.*, 873, 548

## APPENDIX A: MAGNETIC FIELD ABSOLUTE VALUES

As previously described in the text, the mean values of the magnetic field measured on-board were mostly constant through operations. It was only due to some configuration changes in the satellite or due to induced magnetic fields during in-flight experiments that we did observe variations in the mean value of the magnetic field. In order to provide a more quantitative description, we summarize in Table A1 the mean values of the three components of the magnetic field measured on-board for the four magnetometers. We repeated the same analysis for the four different phases that we already distinguished during our analysis, i.e. LTP and DRS nominal and extended operations. For each segment we also provide an estimate of the gradient of the magnetic field across each couple of magnetometers in the X and Y direction. The dates for each subset were selected trying to maximize the amount of data for that segment and trying to avoid any major changes (no experiments, glitches, etc). LTP nominal goes from 2016 March 1 to April 27. LTP extended goes from 2016 December 7 to January 13 and from 2017 January 15 to March 14. The 2 d gap is to get rid of the short DRS period in between. DRS nominal goes from 2016 June 27 to December 7. DRS extended goes from 2017 March 19 to April 28. Errors are computed as  $\sigma/\sqrt{N}$ .

**Table A1.** Mean values of the DC magnetic field for different spacecraft configurations.

Magnetometer	LTP Nominal		LTP Extended	
	$(B_x, B_y, B_z)$ [nT]	$ \vec{B} $ [nT]	$(B_x, B_y, B_z)$ [nT]	$ \vec{B} $ [nT]
PX	$(866.880 \pm 0.005, -908.001 \pm 0.005, 82.053 \pm 0.005)$	$1258.046 \pm 0.009$	$(736.202 \pm 0.006, -896.577 \pm 0.005, 100.497 \pm 0.006)$	$1164.450 \pm 0.010$
MX	$(816.303 \pm 0.005, -457.364 \pm 0.006, 91.730 \pm 0.005)$	$940.184 \pm 0.009$	$(696.128 \pm 0.005, -428.666 \pm 0.005, 94.944 \pm 0.006)$	$823.021 \pm 0.009$
PY	$(-111.894 \pm 0.005, 585.993 \pm 0.005, 384.374 \pm 0.005)$	$709.684 \pm 0.009$	$(-131.575 \pm 0.005, 582.902 \pm 0.005, 394.238 \pm 0.005)$	$715.898 \pm 0.009$
MY	$(-86.583 \pm 0.006, 1023.586 \pm 0.006, 527.776 \pm 0.005)$	$1154.890 \pm 0.010$	$(-109.538 \pm 0.006, 1006.245 \pm 0.006, 541.992 \pm 0.006)$	$1148.165 \pm 0.010$
PX-MX	$(\partial_x B_x, \partial_x B_y, \partial_x B_z)$ [nT/m]	$ \partial_x \vec{B} $ [nT/m]	$(\partial_x B_x, \partial_x B_y, \partial_x B_z)$ [nT/m]	$ \partial_x \vec{B} $ [nT/m]
	$(62.717 \pm 0.006, -611.033 \pm 0.007, -12.544 \pm 0.005)$	$614.371 \pm 0.010$	$(49.694 \pm 0.006, -634.456 \pm 0.006, 7.024 \pm 0.006)$	$636.438 \pm 0.010$
PY-MY	$(\partial_y B_x, \partial_y B_y, \partial_y B_z)$ [nT/m]	$ \partial_y \vec{B} $ [nT/m]	$(\partial_y B_x, \partial_y B_y, \partial_y B_z)$ [nT/m]	$ \partial_y \vec{B} $ [nT/m]
	$(-34.318 \pm 0.006, -542.507 \pm 0.005, -185.989 \pm 0.005)$	$574.529 \pm 0.009$	$(-29.880 \pm 0.006, -524.843 \pm 0.006, -191.632 \pm 0.006)$	$559.532 \pm 0.010$
Magnetometer	DRS Nominal		DRS Extended	
	$(B_x, B_y, B_z)$ [nT]	$ \vec{B} $ [nT]	$(B_x, B_y, B_z)$ [nT]	$ \vec{B} $ [nT]
PX	$(833.375 \pm 0.026, -901.685 \pm 0.004, 60.990 \pm 0.005)$	$1229.337 \pm 0.026$	$(762.165 \pm 0.011, -886.156 \pm 0.007, 79.828 \pm 0.009)$	$1171.555 \pm 0.016$
MX	$(710.415 \pm 0.024, -437.246 \pm 0.006, 87.603 \pm 0.003)$	$838.778 \pm 0.025$	$(634.580 \pm 0.010, -421.112 \pm 0.005, 94.165 \pm 0.006)$	$767.394 \pm 0.013$
PY	$(-124.643 \pm 0.005, 581.454 \pm 0.003, 390.371 \pm 0.003)$	$711.347 \pm 0.007$	$(-118.939 \pm 0.005, 583.369 \pm 0.005, 391.387 \pm 0.006)$	$712.495 \pm 0.009$
MY	$(-102.913 \pm 0.006, 1064.324 \pm 0.006, 531.317 \pm 0.004)$	$1194.016 \pm 0.008$	$(-102.051 \pm 0.008, 1052.539 \pm 0.011, 551.385 \pm 0.008)$	$1192.593 \pm 0.016$
PX-MX	$(\partial_x B_x, \partial_x B_y, \partial_x B_z)$ [nT/m]	$ \partial_x \vec{B} $ [nT/m]	$(\partial_x B_x, \partial_x B_y, \partial_x B_z)$ [nT/m]	$ \partial_x \vec{B} $ [nT/m]
	$(151.504 \pm 0.011, -627.590 \pm 0.018, -34.241 \pm 0.007)$	$646.5250 \pm 0.022$	$(158.210 \pm 0.015, -630.569 \pm 0.006, -18.599 \pm 0.008)$	$650.380 \pm 0.018$
PY-MY	$(\partial_y B_x, \partial_y B_y, \partial_y B_z)$ [nT/m]	$ \partial_y \vec{B} $ [nT/m]	$(\partial_y B_x, \partial_y B_y, \partial_y B_z)$ [nT/m]	$ \partial_y \vec{B} $ [nT/m]
	$(-29.619 \pm 0.005, -596.135 \pm 0.020, -182.260 \pm 0.006)$	$624.078 \pm 0.021$	$(-22.898 \pm 0.010, -581.655 \pm 0.013, -207.513 \pm 0.006)$	$617.987 \pm 0.017$

<sup>1</sup>European Space Technology Centre, European Space Agency, Keplerlaan 1, NL-2200 AG Noordwijk, the Netherlands<sup>2</sup>Albert-Einstein-Institut, Max-Planck-Institut für Gravitationsphysik und Leibniz Universität Hannover, Callinstraße 38, D-30167 Hannover, Germany<sup>3</sup>APC, Paris Diderot University, CNRS/IN2P3, CEA/Irfu, Obs de Paris, Sorbonne Paris Cité 75013, France<sup>4</sup>Department of Industrial Engineering, University of Trento and Trento Institute for Fundamental Physics and Applications/INFN, Via Sommarive 9, I-38123 Trento, Italy<sup>5</sup>Dipartimento di Fisica, Università di Trento and Trento Institute for Fundamental Physics and Applications/INFN, I-38123 Povo, Trento, Italy<sup>6</sup>Istituto di Fotonica e Nanotecnologie, CNR-Fondazione Bruno Kessler, I-38123 Povo, Trento, Italy<sup>7</sup>DISPEA, Università di Urbino ‘Carlo Bo’, Via S. Chiara 27, I-61029 Urbino/INFN, Italy<sup>8</sup>The School of Physics and Astronomy, University of Birmingham, Birmingham B15 2TT, UK<sup>9</sup>European Space Astronomy Centre, European Space Agency, Villanueva de la Cañada, E-28692 Madrid, Spain<sup>10</sup>Institut für Geophysik, ETH Zürich, Sonneggstrasse 5, CH-8092, Zürich, Switzerland<sup>11</sup>The UK Astronomy Technology Centre, Royal Observatory, Edinburgh, Blackford Hill, Edinburgh EH9 3HJ, UK<sup>12</sup>Institut de Ciències de l’Espai (CSIC-IEEC), Campus UAB, Carrer de Can Magrans s/n, E-08193 Cerdanyola del Vallès, Spain<sup>13</sup>European Space Operations Centre, European Space Agency, D-64293 Darmstadt, Germany<sup>14</sup>High Energy Physics Group, Physics Department, Imperial College London, Blackett Laboratory, Prince Consort Road, London SW7 2BW, UK<sup>15</sup>Department of Mechanical and Aerospace Engineering, University of Florida, MAE-A, P.O. Box 116250, Gainesville, FL 32611, USA<sup>16</sup>Physik Institut, Universität Zürich, Winterthurerstrasse 190, CH-8057 Zürich, Switzerland<sup>17</sup>SUPA, Institute for Gravitational Research, School of Physics and Astronomy, University of Glasgow, Glasgow G12 8QQ, UK<sup>18</sup>Department d’Enginyeria Electrònica, Universitat Politècnica de Catalunya, E-08034 Barcelona, Spain<sup>19</sup>National Institute for Astrophysics, Astrophysical Observatory of Torino, Via Osservatorio 20, I-10025 Pino Torinese (TO), Italy<sup>20</sup>Airbus Defence and Space, Gunns Wood Road, Stevenage, Hertfordshire SG1 2AS, UKThis paper has been typeset from a  $\text{\TeX}/\text{\LaTeX}$  file prepared by the author.